(Original Paper)

# Numerical Simulation of the Effect of Free Surface Shape on Marangoni Convection in a Liquid Film Sustained in a Circular Ring with Different Prandtl Numbers

Nikhil ADKAR[1], Takuya YAMAMOTO[1], Youhei TAKAGI[1], Yasunori OKANO[1, 2] and Sadik DOST[2]

**Abstract**

In 2003 NASA astronaut Dr. D. Pettit conducted thermocapillary experiments in a thin water film (Prandtl number; $Pr = 7$) sustained in a circular ring onboard the International Space Station (ISS). When a section of the ring was heated, a thermocapillary flow developed from the cold region towards the hotter region. This unusual flow phenomenon (being from cold to hot) was explained by the dependency of free surface shape on the flow pattern observed in the film. However, the dependency of flow behavior on the Prandtl number was not investigated previously. Motivated by the wide range of applications of the low-Prandtl-number liquids, numerical simulations for the flow phenomena observed in the films of different shapes and Prandtl numbers were performed under zero gravity. Results have shown that in the case of low-Prandtl-number film although the flow direction remained the same, the flow velocity increased significantly. This interesting phenomenon is explained by means of the temperature gradient in the film in the $y$- (vertical) and $\theta$- (circumferential) directions.

## 1. Introduction

Thermocapillary flows are driven by surface tension gradient when a free surface exits[1]. In industrial processes and material processing such as laser welding, drying, coating, crystal growth, surface characteristics of the final product are significantly influenced by thermocapillary flows during the process. The effect of such flows becomes significant particularly in the microgravity environment and also in thin films on Earth[2]. Although the relevant literature is relatively rich on thermocapillary flows in thin films with a single free surface, only a few studies have been reported on liquid films with double free surfaces[3,4].

In the case of a water film, upon the onset of a temperature gradient on the surface, the surface tension at the hotter region decreases and this gives rise to the development of a thermocapillary flow towards the colder region (where the surface tension is higher). However, the direction of the thermocapillary flow observed in Pettit's microgravity experiments onboard the ISS was from the cold side to the hot side of the water film[5]. The ground-based experiments of Kawamura *et al.*[6] in thin films led to the observation similar to that of Pettit's microgravity experiment, when milk powder was added to the film. However, in the experiment with no milk powder the observed flow direction was opposite. Based on these conflicting observations they have concluded that the observed flow pattern from cold to hot in the film was due to evaporation of water. Their 2-D numerical simulations could also not clarify this issue.

Further ground-based experiments by Ueno and Torii[7], Watanabe and Ueno[8] conducted in a rectangular film have suggested that the Marangoni number determines the flow instability and the film volume ratio changed the flow direction in the rectangular films of double free surfaces[7-9]. There are also a few studies examining flow patterns in a circular film[10-12].

Conducting experiments in low-Prandtl-number liquid films has proven challenging due to oxidation of the liquid melt, covering the film surface with a solid oxide layer and making the flow stagnant[13-15]. Similarly, an outward flow was also observed in liquid gallium[13], which was attributed to contaminants and overcooling of gallium.

In our previous study[10], we have established a connection between the changes in the flow patterns and the film shapes. Kuhlmann[16] provided an alternative explanation for such flow patterns.

To shed further light on the flow behavior and also to examine the role of the Prandtl number, we have examined the flow patterns at three different Prandtl number values: namely $Pr = 7$ (high), $Pr$

---

1   Department of Materials Engineering Science, Osaka University, Osaka, Japan.
2   Crystal Growth Laboratory, University of Victoria, Victoria, Canada.
 (E-mail: okano@cheng.es.osaka-u.ac.jp)
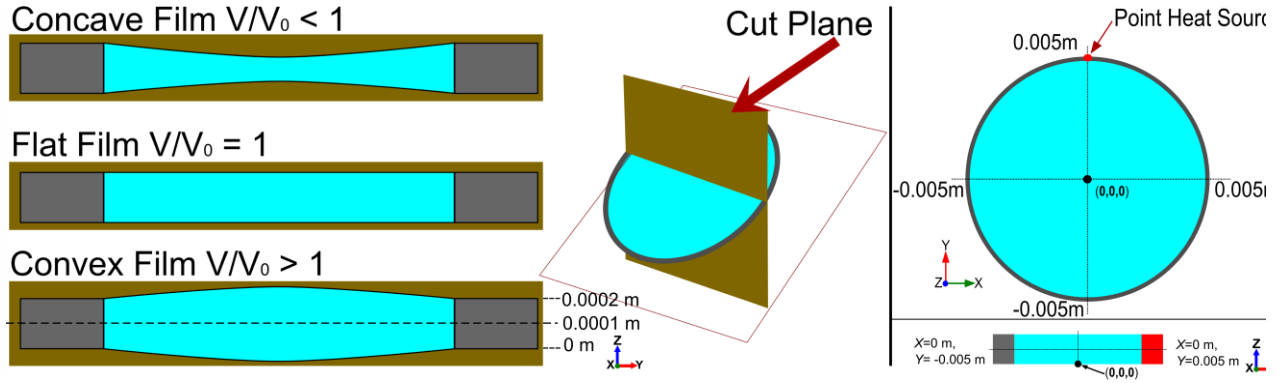
**Fig. 1**    Schematic views of the cross-sections of the computational domain.

= 0.7 (middle) and *Pr* = 0.01 (low). We have carried out numerical simulations for these three cases for concave, flat, and convex films. Our numerical simulations show that the shape of the film plays a critical role in determining the flow velocities in the films. It is shown that the explanation given for the flow directions by means of film volume ratios is also valid at the low Prandtl number.

## 2.    Numerical Analysis

### 2.1    Computational Domain

The schematic views of the computational domains are shown in **Fig. 1**. The shapes of the liquid film free surfaces are characterized by the ratio of $V/V_0$ where $V$ is the volume of the liquid film and $V_0$ is the volume of the liquid film when the free surfaces are flat. In the simulations we used three volume ratio values; namely 0.75 (concave), 1.00 (flat) and 1.25 (convex). The diameter of the film was 10 mm, and the thickness of the water/wire interface was taken as 0.2 mm. A point heat source was assumed as shown in the schematics.

### 2.2    Numerical Assumption

The following assumptions were made in the numerical simulation model.

(1)    The effect of gravity and the contribution of buoyancy driven convection were neglected.

(2)    Heat loss from the solid wire to the ambient gas was neglected.

(3)    All the physical properties except for the surface tension were kept constant and the values at 293 K were used.

(4)    Free surfaces of the thin film do not deform due to fluid flow and were assumed to be adiabatic.

(5)    The ambient gas is passive.

(6)    The temperature field in the ring is independent of the liquid.

The liquid domain in the analysis was assumed to be an incompressible Newtonian fluid. We selected three different values of the Prandtl number representing three classes of liquids: high (*Pr* = 7.00), middle (*Pr* = 0.70) and low (*Pr* = 0.01). The solid wire was assumed to be a heat conducting rigid solid. All the physical properties were the same as used in our previous article[10], except the thermal conductivity of the liquid, $k_L$, and hence the Prandtl numbers were changed from 7.00 ($k_L$ = 0.597 W/(m·K)) to 0.70 ($k_L$ = 5.97 W/(m·K)) and 0.01 ($k_L$ = 415.27 W/(m·K)). The model equations were non-dimensionalized and effect of *Pr* on the flow was studied. This is discussed in section 2.3.

Heat transfer along the solid wire is analytically approximated by using the 1D unsteady state heat conduction. The unsteady function for temperature is obtained as follows:

$$T = T_0 + \frac{q}{A} \cdot \frac{\left(\sqrt{6\alpha t} - r|\theta|\right)^2}{2k\sqrt{6\alpha t}}, |\theta| \leq \sqrt{\frac{6\alpha t}{r}} \qquad (1)$$

$$T = T_0, |\theta| \geq \sqrt{\frac{6\alpha t}{r}} \qquad (2)$$

where $t$ represents time, $\theta$ is the angle, $T$ is temperature, $T_0$ the initial temperature, $\alpha$, $r$, and $k$ are the thermal diffusivity, radius, and thermal conductivity of the wire, respectively, and $q/A$ is the heat flux. The derivation of these equations can be found in Ref.[10]. The shapes of the liquid films were calculated by the Young-Laplace equation. The assumptions of the edge of the film being pinned and the wall being flat and fully wetted were made in calculating the free surface shapes.

### 2.3    Model Equations

The governing equations and the associated boundary conditions of the model were given in our previous work[10]. The model
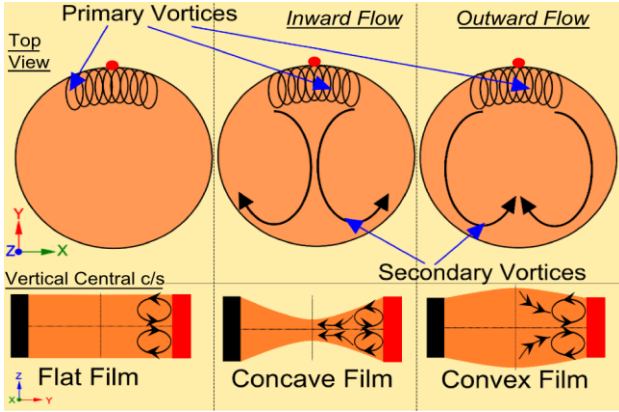
**Fig. 2** Schematics of primary and secondary vortices in different films of high Prandtl number.

equations were non-dimensionalized to show the relationship between $Re$, $Ma$ and $Pr$. The following dimensionless variables were used in the analysis: velocity, $\boldsymbol{u}^* = \boldsymbol{u}\,/U$ ; time, $t^* = t/(d^2/\nu)$ ; temperature, $T^* = (T - T_0)\,/\Delta T_{\max}$ ; pressure, $p^* = p\,/\rho U^2$ ; coordinates $(x, y, z)$, $\boldsymbol{x}^* = \boldsymbol{x}\,/d$, and $U = \sigma_T\, d\,\Delta T_{\max}/\mu D$. Here, $*$ indicates the dimensionless variables, $d$ is the film thickness along the film edge, $\sigma$ is the surface tension of the liquid, $\Delta T_{\max}$ the maximum temperature difference in the film, and $U$ the characteristic thermocapillary velocity. The use of the above dimensionless variables leads to the following dimensionless governing equations:

$$\frac{\partial \boldsymbol{u}}{\partial t} + (\boldsymbol{u} \cdot \nabla)\boldsymbol{u} = -\nabla p + \frac{1}{Re}\nabla^2 \boldsymbol{u} \tag{3}$$

$$\nabla \cdot \boldsymbol{u} = 0 \tag{4}$$

$$\frac{\partial T}{\partial t} + \boldsymbol{u} \cdot (\nabla T) = \frac{1}{Ma}\nabla^2 T \tag{5}$$

where the symbol $*$ was neglected for simplicity, and the relevant dimensionless numbers, namely the thermocapillary Reynolds number $Re$, and the Marangoni number $Ma$ were defined as follows:

$$Re = \frac{\sigma_T \Delta T_{\max} d^2}{\mu \nu D} \tag{6}$$

$$Ma = \frac{\sigma_T \Delta T_{\max} d^2}{\mu D \alpha_L} \tag{7}$$

where, $\sigma_T$ is the surface tension coefficient of temperature, $D$ is the diameter of the film, and $\alpha_L$ and $\mu$ represent the thermal diffusivity

and viscosity of the liquid, respectively. The maximun temperature difference was expressed by[10] :

$$\Delta T_{\max} = \frac{q/A}{k}\sqrt{\frac{3\alpha t}{2}} \tag{8}$$

and,

$$Ma = Re \cdot Pr \tag{9}$$

Substituing the values of $q/A = 1.0 \times 10^4$ W/m$^2$ , $k = 2.00 \times 10^1$ kg·m /(s$^3$·K), $\alpha = 4.40 \times 10^{-6}$ m$^2$/s, we get $\Delta T_{\max}$ as $1.284 \times \sqrt{t}$ K. When $\Delta T_{\max}$ is substituted into Eq. (6) we have $Re$ directly proportional to $\sqrt{t}$. $Re$ can be obtained by substituting values of $\sigma_T = 9.93 \times 10^{-5}$ kg/s$^2$, $\mu = 9.93 \times 10^{-4}$ kg/(m·s), $D = 0.01$ m and $d = 0.0002$ m. These values can be found in Ref.[10].

In this study, we focused on the effect of Prandtl number on the thermocapillary flows developing in thin water film. The Reynolds number was the same in all computations. Hence, by changing $Pr$, $Ma$ was changed and the thermocapillary flows characteristics in the films were investigated. In the subsequent sections, the results will be discussed using dimensional variables.

## 2.4 Numerical Procedure

The governing equations and the boundary conditions were discretized by the finite volume method and the velocity and pressure fields were coupled by the PISO algorithm[17). The values on the cell interfaces were calculated by second order central difference scheme. The first order implicit Euler method was used for the discretization of time derivatives. The time step used was $10^{-4}$ s. Simulations were carried out using the OpenFOAM package (an open source CFD software package developed by OpenFOAM Ltd. at ESI group and distributed by the OpenFOAM Foundation)[18).

## 2.5 Verification of the Numerical Code

The verification of the numerical code was done in our previous work[10, 19). At the low Prandtl number, since the thermal boundary layer thickness gets larger we will not observe the occurrence of a steep temperature gradient. Thus, no further grid refinement was needed; thus the same grid resolution of our previous work[10] was also used here. The total number of grid points is about 240,000 (for flat films) – 590,000 (for non-flat films). The simulations were carried out for 10 seconds.

## 3. Results and Discussion

### 3.1 Flow Patterns

Numerical simulations were conducted for convex, flat and

concave films at high (7.00), middle (0.70) and low (0.01) Prandtl number values. In our previous work with the high-Prandtl-number films we observed the formation of primary and secondary vortices in the deformed (non-flat) films, and only primary vortices in the flat film[10]. These differences in the flow patterns (flow directions) were due to the film geometry. The schematics of the computed flow patterns are shown in **Fig. 2**. As seen, the flow directions of the secondary vortices were inward (from the heated boundary towards inside) in the concave film, and were outward (from inside towards the heated boundary) in the convex film.

Computed flow patterns for three film geometries at three Prandtl number values are presented in **Fig. 3**. Patterns were obtained by placing the particle tracing seeds on the film surface and then by tracking their motions. As seen from the figure, the flow patterns are similar to those obtained in Ref.[10] for all three values of the Prandtl number; namely only primary vortices develop in the flat film (**Fig. 3(a)**) while both primary and secondary vortices occur in the concave and convex films, being inward in the concave film (**Fig. 3(b)**) and outward in the convex film (**Fig. 3(c)**). Detailed discussion on the development of these flow patterns can be found in Ref.[10].
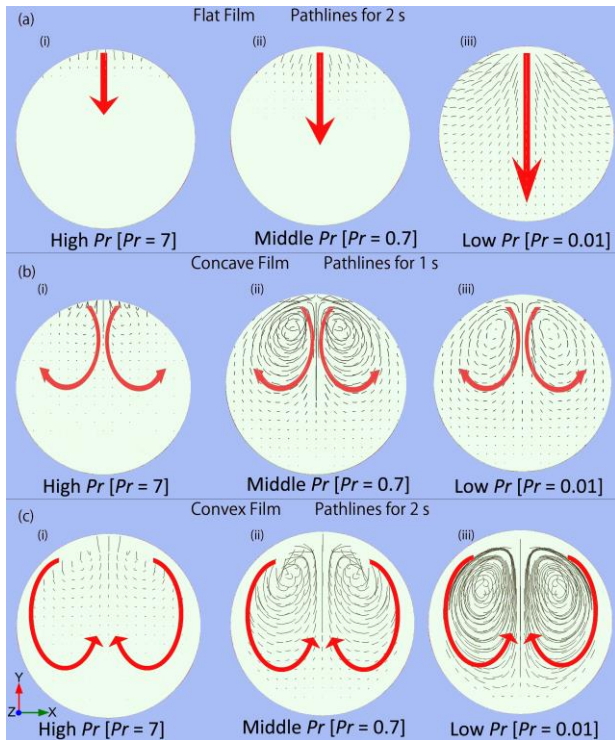


**Fig. 3** Pathlines in different films (seeds of pathlines are initially fixed on the surface of the film) (a) in flat film for 2 seconds (b) in concave film for 1 second and (c) in flat convex films for 2 seconds of (i) high (ii) middle, and (iii) low Prandtl-number films.

## 3.2 Flow Velocity

Normally, thermocapillary flows get weaker (smaller flow velocity) with decreasing temperature gradient when viscosity is kept constant; as its driving force gets weaker. At the low-Prandtl-number values, the temperature gradient in the film is smaller thus a weaker flow (lower velocity) is expected. This is the case in the flat film. However, the computed flow patterns show the opposite in the non-flat films as seen from **Fig. 3**. The flow strengths are higher at the low-Prandtl-number values. This observation is discussed in the next section. In discussing the flow velocity in this article, we mean the absolute velocity, |*U*|. In the next three sections, in (i) – (iii), we compare the maximum absolute velocity in the entire film with time in the case of flat film in (i) and the absolute velocity sampled at the film surface center with time in (ii) and (iii).

### 3.2.1 Cause for Variation of Flow Velocity

In the flat film, initially heat is transferred into the film by conduction[12]. This develops a temperature gradient, and as a result, the primary vortices are generated as shown schematically in (**Fig. 2**). This is explained in detail by means of the heat penetration distance, $\delta$, which is given in the case of flat film by, $\delta = \sqrt{6\alpha_L t}$ , ($\alpha_L$ being the thermal diffusivity of liquid) in Ref.[12]. Then, the developed primary vortices give rise to a convective heat transfer in the film.

On the other hand, in the films with non-flat surfaces, due to curved surfaces and the secondary vortices which develop in the film, the temperature gradient which develops along the film surfaces changes with the shape of the films; contrary to what is seen in the case of flat film. The curvature of film surfaces thus gives rise to steeper temperature gradients in the vertical (*y*) and circumferential (*θ*) directions.

**(i) Increasing flow velocity with increasing *Pr* in flat film**

In the case of flat film, the heat penetrating into the film of high Prandtl number develops a steeper temperature gradient within a short distance from the heating edge (within a narrower region), while in the lower-Prandtl-number films the development of the temperature gradient is gradual, and it takes place within an extended distance from the heated edge (within a wider region). Thus the steeper temperature gradient in the high-Prandtl-number film leads to a stronger thermocapillary flow and naturally to higher flow velocity in the film. However, since the temperature gradient develops within a narrower region, it gives rise to primary vortices within this region (as far as the temperature gradient extends), and the flow velocity becomes zero where the temperature gradient vanishes. The velocity distribution in the film at *t* = 5 seconds is shown in **Fig. 4(a)**.

The maximum flow velocity in the film is plotted against time in

**Fig. 4(b)**. It can be seen from the figure that the maximum velocity is the highest for all times in the high-Prandtl-number film and lowest for the low-Prandtl-number film. In the case of lower-Prandtl-number films, since the lower temperature gradients were developed within a wider region, the primary vortices with lower velocities are formed with longer length in the film. It can also be clearly observed from the particle pathlines in the flat film in **Fig. 3(a)** that the lengths of the primary vortices are longer in the case of low-Prandtl-number film than those in the high-Prandtl-number film. In summary, in the flat film, the flow velocity increases with increasing *Pr*, and the length of the primary vortices decreases.

**(ii) Increasing flow velocity with decreasing *Pr* in a concave film**

The temperature gradient near the heated edge gives rise to the development of the primary vortices in the film. Then, the secondary vortices develop. The secondary vortices can be seen in **Fig. 3(b)**. The flow is in the vertical (*y*) direction from the heated boundary (inward flow). Hence, in the case of concave film, due to the curvature of the film, the temperature gradient in the vertical direction $\partial_y T$ drives the inward flow. To compare velocities of the secondary vortices in the concave film with different Prandtl
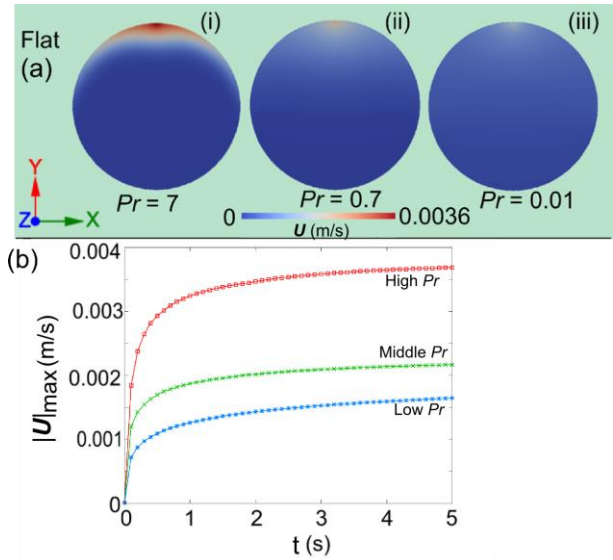


**Fig. 4** Flow velocity in flat films: (a) velocity distribution along the free surface at $t = 5$ seconds (i) high (ii) middle, and (iii) low Prandtl number and (b) time progress of maximum velocity.
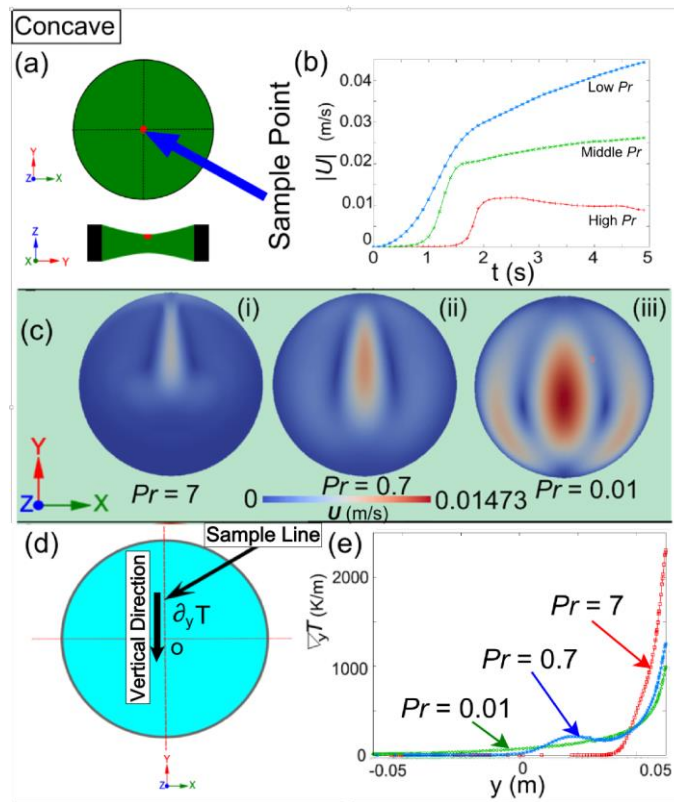


**Fig. 5** Flow velocity in concave films: (a) schematics of the sampled point for velocity, (b) variation of velocity at the sampled point with time, (c) velocity distribution along the free surface at $t = 5$ seconds, (d) schematics of the sampled $\partial_y T$ on the surface along the *y* coordinate and (e) distribution of $\partial_y T$ along the *y* coordinate on the surface.

number values, the center point on the surface was taken as a reference point and the velocities were plotted against time for 5 seconds as shown schematically in **Fig. 5(a)** and plotted in **Fig. 5(b)**. As seen from this figure the film of low *Pr* has a higher flow velocity than those in the middle- and high-Prandtl-number films. The velocity distribution in the films at $t = 5$ seconds is shown in **Fig. 5(c)**.

Since the flow starts in the vertical ($y$) direction, $\partial_y T$ determines the velocity of this flow. Therefore, to compare $\partial_y T$ in the concave films, as shown schematically in **Fig. 5(d)**, the surface was sampled at $x = 0$ for temperature gradient in the $y$ direction ($\partial_y T$) at $t = 1$ second and these values were plotted against the $y$ coordinate at $x = 0$ in **Fig. 5(e)**.

Initially, the flow starts in the vertical direction due to the shape of the film as shown in **Fig. 3(b)**. Then the temperature gradient in the vertical ($y$) direction drives this flow. It can be seen from **Fig. 5(e)** that initially $\partial_y T$ is steeper for high-Prandtl-number film compared with that in the middle-and low-Prandtl-number films, but drops

down to zero after a small distance from the heating edge (heating edge is at $y = 0.05$ m). But in the case of middle- and low-Prandtl-number films, $\partial_y T$ continues to sustain with a moderate value for a longer distance. In all the cases of different Prandtl number values, $\partial_y T$ for some distance from the heating point generates the primary vortices. Therefore, only the small $\partial_y T$ drives the secondary vortices in the case of high-Prandtl-number film. Hence, the flow velocity is small in the high-Prandtl-number film. On the other hand, $\partial_y T$ is much larger in the low-Prandtl-number film and thus gives rise to faster secondary vortices after the generation of primary vortices. Hence, the flow velocity is higher in the low-Prandtl-number film.

**(iii) Increasing flow velocity with decreasing *Pr* in a convex film**

Similar to the concave film, the temperature gradient near the heated edge develops the primary vortices, and then the curvature of the film generates the secondary vortices. In this case, the flow direction is from the inside of the film towards the heated boundary (outward flow), as seen from **Fig. 3(c)**. In the case of a convex film, the temperature gradient in the circumferential direction drives this
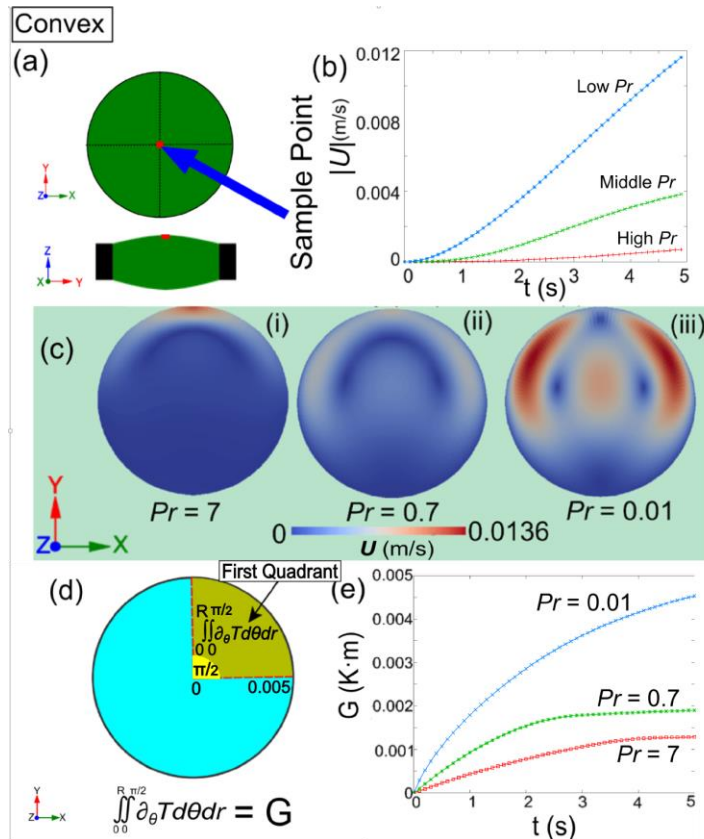


**Fig. 6** Flow velocity in concave films: (a) schematics of the sampled point for velocity, (b) variation of velocity at the sampled point with time, (c) velocity distribution along the free surface at $t = 5$ seconds (i) high (ii) middle, and (iii) low Prandtl number, (d) schematics of the integrated $\partial_\theta T$ is shown (also defined by G) for the first quadrant on the surface and (e) variation of G (integrated $\partial_\theta T$ over first quadrant) on surface of with time.

flow circumferentially. To compare the velocities of the secondary vortices in the convex film with different Prandtl numbers, similar to the previous case, the center point on the surface was taken as a reference point and the velocities were plotted against time for 5 seconds, which is shown schematically in **Fig. 6(a)** and plotted in **Fig. 6(b)**. Similar to the concave film, the flow velocity is higher in the low-Prandtl-number film compared with that of the middle-and high-Prandtl-number films. The velocity distribution in the films at $t = 5$ seconds is shown in **Fig. 6(c)**.

In this case, the flow starts initially in the circumferential ($\theta$) direction unlike the concave film **(Fig. 3(c))**. The strength of the flow in the circumferential direction depends on the temperature gradient in the circumferential direction ($\partial_\theta T$). Unlike the previous case, it is difficult to get a clear idea if $\partial_\theta T$ was plotted against the circumferential coordinates, $\theta$. Therefore, $\partial_\theta T$ on the surface was integrated over the first quadrant (only first quadrant because the values would cancel each other due to symmetry if integrated over the entire circle) of the circle as shown in **Fig. 6(d)** for different time intervals. Also, in **Fig. 6(d)**, this integrated value of $\partial_\theta T$ over the first quadrant is defined by the variable $G$ for simplicity. Then a graph of $G$ was plotted against time for 5 seconds as shown in the **Fig. 6(e)**. It can be observed from this graph that the integrated value of $\partial_\theta T$ was higher for the low-Prandtl-number film than that of the high-Prandtl-number film. This means that the driving force was higher in the case of the low-Prandtl-number film in the circumferential direction which generates a faster flow.

## 4. Conclusion

Convex, concave and flat films of high, middle and low Prandtl number values were numerically simulated to observe and study the thermocapillary flow phenomena observed in microgravity experiments. It was shown that the flow direction remains the same even in the low-Prandtl-number film as in the high-Prandtl-number films. However, the flow velocities change with the film surface shape and the Prandtl number of the liquid. The flow velocity increases with increasing Prandtl number in the case of flat film and the length of the primary vortices increase with decreasing Prandtl number. However, the flow velocity increases with decreasing Prandtl number in the non-flat films. The reasons for stronger flows in the flat and non-flat films are explained. It was shown that the film shape plays a major role in determining the flow direction even in the low-Prandtl-number liquids and in changing the flow velocity in the films with different Prandtl numbers.

## References

1)   L. E. Scriven and C. V. Sternling: Nature, **187** (1960) 186.
2)   M. F. Schatz and G. P. Neitzel: Annu. Rev. Fluid Mech., **33** (2001) 93.
3)   A. K. Sen and S. H. Davis: J. Fluid Mech., **121** (1982) 163.
4)   Y. Chen, S. A. David, T. Zacharia and C. J. Cremers: Num. Heat Transfer A, **33** (1998) 599.
5)   D. Pettit: Saturday Morning Science Videos (2003) see http://mix.msfc.nasa.gov/IMAGES/QTVR/0601211.mov.
6)   H. Kawamura, K. Iwamoto and M. Harashima: J. Jpn. Soc. Microgravity Appl., **23** (2006) 157 (in Japanese).
7)   I. Ueno and T. Torii: Acta Astronaut., **66** (2010) 1017.
8)   I. Ueno, T. Watanabe and T. Katsuta: Thermocapillary-driven flow in a free liquid film, Proc. of Int. Symp. Turbul. Shear Flow Phenom., **2**, Ottawa, Canada, 2011, 1.
9)   I. Ueno, T. Katsuta and T. Watanabe: Flow patterns induced by thermocapillary effect in thin free liquid film accompanying with static/dynamic deformations, Proc. of the second European Conference on Microfluidics, **10**, Toulouse, France, 2010, 203.
10)  T. Yamamoto, Y. Takagi, Y. Okano and S. Dost: Phys. Fluids, **25** (2013) 082108.
11)  T. Yamamoto, Y. Takagi, Y. Okano and S. Dost: Trans. JSASS Aerospace Tech. Japan, **12** (2014) Pe_19.
12)  T. Yamamoto, Y. Takagi, Y. Okano and S. Dost: J. Chem. Eng. Jpn., **48** (2015) 407.
13)  J. Priede, A. Cramer, A. Bojarevics, A. Y. Gelfgat, P. Z. Bar-Yoseph, A. L. Yarin and G. Gerbeth: Phys. Fluids, **11** (1999) 3331.
14)  T. Azami, S. Nakamura and T. Hibiya: J. Cryst. Growth, **223** (2001) 116.
15)  K. Takagi, M. Otaka, H. Natsui, T. Arai, S. Yoda, Z. Yuan, K. Mukai, S. Yasuhiro and N. Imaishi: J. Cryst. Growth, **233** (2001) 399.
16)  H. C Kuhlmann: Microgravity Sci. Technol., **26** (2014) 397.
17)  R. I. Issa: J. Comput. Phys., **62** (1986) 40.
18)  See http://www.openfoam.com for the open source CFD toolbox, OpenFOAM.
19)  Y. Takagi, Y. Okano, H. Minakuchi and S. Dost: J. Cryst. Growth, **385** (2014) 72.